

Visualizing the interplay of Dirac mass gap and magnetism at nanoscale in intrinsic magnetic topological insulators

Mengke Liu¹, Chao Lei¹, Hyunsue Kim¹, Yanxing Li¹, Lisa Frammolino¹, Jiaqiang Yan², Allan H. Macdonald^{1*}, Chih-Kang Shih^{1*}

¹ Department of Physics, The University of Texas at Austin, Austin, TX 78712, USA

² Materials Science and Technology Division, Oak Ridge National Laboratory, Oak Ridge, TN 37831, USA

* To whom correspondence may be addressed.

Email: macdpc@physics.utexas.edu or shih@physics.utexas.edu.

Abstract

In intrinsic magnetic topological insulators, Dirac surface state gaps are prerequisites for quantum anomalous Hall and axion insulating states. Unambiguous experimental identification of these gaps has proved to be a challenge, however. Here we use molecular beam epitaxy to grow intrinsic MnBi₂Te₄ thin films. Using scanning tunneling microscopy/spectroscopy, we directly visualize the Dirac mass gap and its disappearance below and above the magnetic order temperature. We further reveal the interplay of Dirac mass gaps and local magnetic defects. We find that in high defect regions, the Dirac mass gap collapses. *Ab initio* and coupled Dirac cone model calculations provide insight into the microscopic origin of the correlation between defect density and spatial gap variations. This work provides unambiguous identification of the Dirac mass gap in MnBi₂Te₄, and by revealing the microscopic origin of its gap variation, establishes a material design principle for realizing exotic states in intrinsic magnetic topological insulators.

Main Text

Introduction

In magnetic topological insulators (MTI), time-reversal symmetry breaking opens a surface state Dirac mass gap that is a prerequisite for realizing quantum anomalous Hall (QAH) and axion insulator ground states (1-3). QAH states support spin-momentum locked dissipationless edge states that hold great promise in advancing electronic and spintronic device applications. Early materials design was based on doping topological insulators with magnetic elements (4, 5); however, dopant disorder (6, 7) is significant and considered to be the main cause for quantized edge states being observed only at extremely low temperature, ~ 30 mK in chromium-doped $(\text{Bi,Sb})_2\text{Te}_3$ (5). Recently a new family of intrinsic MTIs based on layered van der Waals material MnBi_2Te_4 has emerged, in which an ordered Mn magnetic layer is incorporated stoichiometrically in the middle of each van der Waals layer (8-14), suppressing the disorder effect. Indeed, the QAH effect has been observed in MnBi_2Te_4 at a significantly higher temperature of 1.4 K (15). However, the QAH effect is not always observed, even in samples that appear similar (16-20). Moreover, observations of the Dirac mass gap, a prerequisite for the QAH effect and a direct consequence of exchange coupling between the Dirac surface state and the spontaneous magnetization (21, 22), has proven to be challenging and remained unclear (9, 23-30). Given the significant fundamental and application interest in this system, addressing the elusive nature of the Dirac mass gap becomes ever more critical.

Current bulk MnBi_2Te_4 samples are known to be heavily degenerate n-type, with Fermi level (E_F) located deeply inside the conduction band (9, 23-26). As a result, short Dirac fermion lifetimes smear gap signatures. Besides, defects distribution inhomogeneity can complicate the magnetic

order (30-32) and impact the exchange gap distribution (6, 32-37). Spatial fluctuations of chemical potential and another chemical composition mixing, such as Bi_2Te_3 and MnTe_2 (16, 17, 38), further entangle the electronic structure and complicate the gap observation. Thus, to properly address the nature of Dirac mass gap, a microscopic characterization based on intrinsic samples with Fermi level lies within the Dirac gap is crucial.

Here we achieve successful layer-by-layer growth of MnBi_2Te_4 thin film on HOPG and graphene substrate using molecular beam epitaxy (MBE). Furthermore, we control the defect concentration such that E_F lies inside the Dirac gap. Using *in situ* scanning tunneling microscopy/spectroscopy (STM/S), we directly observed the Dirac mass gap and its variation as a function of film thickness and the magnetic antisites concentrations. We found that in high defect regions, the Dirac mass gap collapses. To understand these phenomena, we combine *ab initio* supercell calculation with the coupled Dirac cone model to account for the effect of magnetic antisites defects and successfully demonstrate the Dirac mass gap fragility to antisites. Our calculation predicts maximum antisite densities for observing the QAH effect. This work provides unambiguous evidence for the presence of a Dirac mass gap in intrinsic MTI and reveals the microscopic origin for the gap variation. It further establishes magnetic defect as a critical tuning knob in controlling the topological phases of MTI for QAH and axion insulator-based device applications.

Bulk crystals versus MBE grown thin films

MnBi_2Te_4 is a layered van der Waals material consisting of Te-Bi-Te-Mn-Te-Bi-Te septuple layers (SLs), in which the Mn atomic layer is coupled ferromagnetically within the SL and antiferromagnetically with neighboring SLs. The lattice illustration shown in Fig. 1A includes two commonly observed native defects, Mn_{Bi} and Bi_{Te} antisites. STM images taken on the cleaved

bulk crystals (Fig. 1B) show $\sim 5\%$ Mn_{Bi} antisites, which appear as dark triangular depressions (39), and $\sim 0.2\%$ of Bi_{Te} antisities which appear as bright circular protrusions (39). The abundance of the Bi_{Te} antisities is related to the Te content during the growth (40). The broad background fluctuation may reflect an inhomogeneous distribution of the Bi_{Mn} antisite, the most common n-type dopant (40), located at the Mn layer and is too far from the surface to be directly imaged by STM. But its high concentration is expected from the internal strain energy in the middle Mn layer [40] and can be inferred from the heavily degenerate n-type nature of the sample. As shown in Fig. 1C, we find that E_F is 0.28 eV above the Dirac point in bulk samples, consistent with previous ARPES results (9, 23-25). However, the Dirac gap signature is smeared and difficult to quantify.

We succeed in growing MnBi_2Te_4 thin films on the HOPG and the graphene substrates. The STM/S results reported here are primarily carried out on samples grown on HOPG substrate. A typical STM image of our MBE-grown MnBi_2Te_4 flakes, shown in Fig. 1D, demonstrates SL-by-SL growth of high-quality MnBi_2Te_4 thin film. A topographic section across the flakes (Fig. 1E) allows us to determine the thickness in terms of the number of SLs. This thickness determination is crucial because it eliminates the possibility of Bi_2Se_3 or MnTe_2 intermixing, which would lead to different layer thicknesses. (Additional topographic images of MBE grown samples can be found in Supplementary Fig. S1.) Fig. 1D inset shows the corresponding atomic image, exhibiting $\sim 4\%$ of Mn_{Bi} antisites and no bright Bi_{Te} antisities. The disappearance of Bi_{Te} antisities is due to a Te-rich growth ambient which also reduces the Bi_{Mn} antisites (40). Most importantly, in the ultra-thin regime, the internal energy in the Mn layer may not yet build up significantly, thus delaying the strain compensation effect through Bi_{Mn} antisites (40). The clean and flat background of the atomic image reflects a considerably reduced concentration of Bi_{Mn} antisites. The SL-by-SL MBE

growth of MnBi_2Te_4 films with low defect density we report provides access to the rich electronic properties of MnBi_2Te_4 thin films.

Direct observation of Dirac mass gaps

We start with the 4 SL film, thick enough that its topological surface state is well-developed. Fig. 2A shows a typical tunneling spectrum acquired at 4.3 K at a relatively high setpoint bias of 0.6 V. In this spectrum, there exists a sizeable low-conductance bias range from -0.3 V to +0.4 V, marked by the blue and orange arrows. This low conductance region is due to a significantly reduced density of state (DOS). We find that with a lower setpoint bias as shown in Fig. 2B for which the tip-to-sample distance is reduced, states near E_F can be well resolved. The behavior of bias-dependent tip-to-sample distance can be found in Supplementary Fig. S2, and the tunneling junction characteristics (barrier height) at different biases can be found in Supplementary Fig. S3. In Fig. 2B, which focuses on states near the Fermi energy, one can observe a clear exchange gap of ~ 120 meV with E_F located 20 meV below the conduction band edge.

We further carried out the STS measurement at 77 K, a temperature above the Neel temperature. At a high setpoint bias (Fig. 2C), the spectrum exhibits a low conductance region from -0.3 V to 0.4 V, similar to that acquired in Fig. 2A. With a low setpoint bias (Fig. 2D), the electronic states near the Fermi level can be clearly observed. However, the gap disappears. This direct comparison further affirms that the observed gap at 4.3 K is the Dirac mass gap due to the exchange interaction of the Dirac surface states with the spontaneous magnetization below the Neel temperature.

Fig. 2E shows theoretical projected density-of-states (DOSs) curves for the top four atomic layers of a defect-free 4 SL MnBi_2Te_4 thin film. These results show a ~ 0.45 eV low DOS energy range (marked between the blue and orange arrows), in agreement with our experimental observed low

conductance region of 0.7 eV. The true theoretical Dirac mass gap within which the DOS vanishes is only 48 meV for a 4 SL film. Fig. 2F summarizes the STS-measured (See Supplementary Fig. S4 for 1 to 3 SL STS) and the density-functional theory (DFT)-calculated (Supplementary Fig. S5) energy gap as a function of the thickness, which shows excellent overall agreement, given the known tendency toward bandgap under-estimation in DFT. Our gap determinations have been cross-checked by obtaining STS data at different temperatures and in several different measurement modes (Fig. S2 and S3). This provides unambiguous evidence of the Dirac mass gap in intrinsic magnetic topological insulators, resolving current debates (9, 21, 23-28).

Role of magnetic antisite defects

The thickness-dependent STS measurements discussed above were carried out in low defect areas, where STS shows consistent uniform gap values. We next discuss how defects impact the local electronic structure. Fig. 3A shows a region with low Mn_{Bi} antisites (< 4%) on 4 SL MnBi_2Te_4 . Fig. 3B displays spatial dependent tunneling spectra. Depending on their specific locations, the tunneling peak features show intensity variation. However, the spectra exhibit a uniform gap value with E_{F} located within the gap. Note that the intrinsic nature of this sample suggests a similar amount of Bi_{Mn} antisite (n-type dopant) and Mn_{Bi} antisite (p-type dopant). This situation changes drastically in high defective areas. Fig. 3C shows the atomic image of the defective area on 3 SL MnBi_2Te_4 , exhibiting high concentrations of Mn_{Bi} (~ 9%). In such areas, locally “defect-free” regions on the scale of 2 nm by 4 nm can be found. Fig. 3D shows a sequence of spectra from points between the locally defect-free region (location #1) and the defective area. The spectrum at position #1 exhibits a finite Dirac gap, whose tunneling features are similar to those on the clean area (Supplementary Fig. S4C). As one progresses to a defective area, the Dirac gap decreases

(position #2) and eventually collapses (#3 to #6) with a V-shape DOS suggesting the recovery of the linear Dirac dispersion. Interestingly, in the spectra acquired in the defective region (#3 to #6), one observes an additional zero-bias anomaly, characterized by a dip at zero bias and two peaks at ± 6 meV. We attribute this zero-bias anomaly to inelastic scattering due to spin excitations, similar to those reported previously in other systems (41-43), further confirming the magnetic nature of the Mn_{Bi} antisites. The evolution of the Dirac mass gap observed here strongly suggests the significance of defects concentration, particularly magnetic antisites, in suppressing the exchanging coupling between the Dirac surface states and the magnetic moments.

***Ab initio* DFT and coupled Dirac cone model calculations**

Motivated by our experimental observations, we performed DFT supercell calculation to account for the role of defects and interpreted them using a simplified Dirac-cone model (22) of the MnBi_2Te_4 electronic structure. Fig. 4A illustrates the magnetic moments and exchange couplings present in our model calculation. The Mn_{Bi} antisites moments have been shown to be antiparallel to those in the central Mn layer (31). Exchange interactions between Fermi level electrons and these moments partially cancel those from the central Mn layer, reducing the same-septuple-layer and neighboring-septuple-layer exchange couplings J_s and J_D (See Supplementary Fig. S6 for detailed definition.). To estimate the change of J_s and J_D as a function of magnetic antisites density, we perform DFT supercell calculations for bulk MnBi_2Te_4 crystals that have a ferromagnetic spin configuration and varying antisite defect configurations. A $4 \times 4 \times 1$ superstructure with one Mn_{Bi} antisite per sixteen Bi atoms is used to simulate 6% Mn_{Bi} (see Supplementary Fig. S7 for other superstructure configurations). To keep the chemical potential within the gap, we choose to compensate the Mn_{Bi} antisite with a Bi_{Mn} antisite by substituting the

Bi atom with its next nearest-neighbor Mn atom, as illustrated in Fig. 4A. This antisite pair configuration has the lowest formation energy (31). The presence of Bi_{Mn} antisites also decreases J_S by reducing the magnetic moment in the Mn layer. As shown in Fig. 4B, bulk MnBi_2Te_4 with a ferromagnetic spin configuration is a topological Weyl semimetal (red curve). This topological phase is destroyed by 6% Mn_{Bi} , leading to a trivial insulating state (black curve).

We also calculate other defect concentrations to learn the evolution of electronic structure as defect density varies. Fig. 4C (red curve) summarizes the DFT calculated Γ point energy gap as a function of defect density, showing a gap closing at around 2% Mn_{Bi} at which a topological phase transition from a Weyl semimetal to a trivial insulator occurs and illustrating the sensitivity of the topological phase of ferromagnetic bulk MnBi_2Te_4 to Mn_{Bi} concentration. Following a procedure similar to that employed in Ref.22 key model parameters, such as the exchange potential strength m_F which is equal to sums and differences of J_S and J_D in the ferromagnetic and antiferromagnetic configurations, can be readily extracted from parallel-spin-configuration DFT energy bands. Fig. 4C (blue curve) plots the defect density dependence of m_F , showing that it decreases nearly linearly with an increase of defect density. In Fig. 4C we normalize m_F relative to the same-layer and adjacent-layer Dirac cone hybridization parameters Δ_S and Δ_D . (A detailed explanation of these parameters can be found in Supplementary Fig. S6.)

Using the parameters extracted from DFT, we performed coupled Dirac cone model calculations for thin films with antiferromagnetic spin-configurations. Fig. 4D summarizes the calculated Γ point energy gaps for both spin-aligned bulk and antiferromagnetic thin film cases. The bulk results (dashed black line) agree well with the DFT results (gold diamonds), confirming the validity of our model. For antiferromagnetic thin films such as 4 and 6 SLs, gaps can be suppressed by half

with less than 6% Mn_{Bi} . As is expected [44] (see supplementary Fig. S8 for detailed discussion), this effect is even more dramatic for odd SLs, as exemplified by the 3 and 5 SLs results in Fig. 4D. In that case, gap values show a linear dependence on the defect density, and a topological phase transition occurs at around 1% for 3 SL and 6% for 5 SL thin films. A turning point occurs at about 9% due to the exchange coupling contributed by the Mn_{Bi} overtaking that by the central Mn layer. This eventually leads to a second gap crossing zero accompanied by a trivial insulator to Chern insulator transition with the opposite relationship between Chern number and magnetization. The gap quenching defect concentration (1%) is small for 3 SL MnBi_2Te_4 in our model calculations because of accidental proximity to a topological phase transition (22). However, the experimental Dirac mass gap for 3 SL is larger than that in the model calculation. Thus, its gap quenching should occur at a higher defect concentration.

This model captures the variation of the Dirac mass gap as the magnetic antisite density increases but neglects the antisites-induced disorder effect. In practice, observation of the QAH effect will require even lower Mn_{Bi} antisite densities than those predicted here. Current bulk MnBi_2Te_4 has a 3% to 6% Mn_{Bi} (26, 33, 39, 45) (10% to 20% of Mn_{Sb} for MnSb_2Te_4 (31, 32)) concentration. A large density of Bi_{Mn} antisites can also be inferred from the heavily degenerate n-type nature of the material. Considering the disorder effect, it is understandable why the QAH effect is not universally observed in an odd-SL MnBi_2Te_4 thin-film (16, 17, 19, 20, 46).

Our experimental STM/S study of intrinsic MBE-grown MnBi_2Te_4 thin films provides unambiguous evidence for a Dirac mass gap in regions with low magnetic antisite defect density and resolves the current debate as to whether or not the topological surface states are gapped. STS spatial mapping across boundaries between pristine and defective regions directly reveals how

Mn_{Bi} defects suppress the Dirac mass gap. *Ab initio* DFT and coupled Dirac cone model calculations unveil the microscopic mechanism for this correlation. The model calculations predict critical antisite densities above which the QAH effect cannot be observed in the antiferromagnetic MnBi₂Te₄ thin films (~6% for 5 SL films). By demonstrating the microscopic origin of the Dirac mass gap variation in MnBi₂Te₄, our work establishes magnetic defect as an important parameter in controlling the topological quantum phases.

Materials and Methods

Sample growth and STM/STS measurements

MnBi₂Te₄ thin films were grown in a home-built MBE chamber with base pressure at $\sim 10^{-10}$ torr. High-oriented pyrolytic graphite (HOPG) substrates were cleaved in air and immediately transferred into the MBE chamber. HOPG substrates were outgassed at ~ 300 °C overnight before the growth of MnBi₂Te₄. High-purity Mn (99.99%), Bi (99.999%), and Te (99.999%) were evaporated from standard Knudsen cells. Samples were grown at 240 °C and post-annealed at the growth temperature in a Te ambient. Samples were transferred from the MBE chamber into the STM chamber, with base pressure $\sim 10^{-11}$ torr, through a transfer vessel, with base pressure $\sim 10^{-10}$ torr, to maintain the cleanness of the film. STM/STS measurements were conducted at 4.3 K. The W tip was prepared by electrochemical etching, and then cleaned by *in situ* electron-beam

heating. STM dI/dV spectra were measured using a standard lock-in technique with feedback loop off, whose modulation frequency is 490 Hz.

Ab initio DFT calculations

DFT calculations were performed using Vienna *Ab initio* Simulation Package (VASP) (47) in which generalized gradient approximations (GGA) of Perdew-Burke-Ernzerhof (PBE) (48) have been adopted for exchange-correlation potential. On-site correlation on the Mn-3d states is treated by performing a simplified (rotationally invariant) approach to the LSDA+U calculations (49) with $U - J$ equals 5.34 eV. U and J represents the strength of the effective on-site Coulomb and exchange interactions. A 20 Å of vacuum is used when calculating the MnBi_2Te_4 thin films to avoid the periodic image interactions normal to the surface. The global break condition for the electronic self-consistency loop is set to be 10^{-7} eV, and the plane wave energy cutoff is set to be 600 eV. DOS in Fig. 2E are calculated on a $16 \times 16 \times 1$ Γ -centered k-point integration grid with a Gaussian broadening factor of 50 meV.

Supercells that correspond to $3 \times 3 \times 1$ and $4 \times 4 \times 1$ of the original primitive cell were used to simulate the antisite defects in the ferromagnetic configuration. As illustrated in Fig. S7, one Mn_{Bi} antisite per sixteen Bi atoms in a $4 \times 4 \times 1$ supercell corresponds to Mn_{Bi} density of 1/16; one Mn_{Bi} antisite per nine Bi atoms in a $3 \times 3 \times 1$ supercell corresponds to Mn_{Bi} density of 1/9; two Mn_{Bi} antisites per sixteen atoms in a $4 \times 4 \times 1$ supercell corresponds to Mn_{Bi} density of 1/8. The global break condition for the electronic self-consistency loop is set to be 10^{-6} eV, and a $9 \times 9 \times 3$ Γ -centered k-point integration grid was employed.

Acknowledgments

This work was primarily supported by the National Science Foundation (NSF) through the Center for Dynamics and Control of Materials: an NSF MRSEC under cooperative agreement no. DMR-1720595 and the US Air Force grant no. FA2386-21-1-4061. Other supports were from NSF grant nos. DMR-1808751, the Welch Foundation F-1672. Work at ORNL was supported by the U.S. Department of Energy, Office of Science, Basic Energy Sciences, Materials Sciences and Engineering Division. We thank C.Z. Chang for the helpful discussion in MBE growth.

Author Contributions

M.L. and C.-K.S. designed the research. M.L., Y.L., and L.F. performed the STM/STS study. H.K. and M.L. carried out the MBE growth. C.L. performed the theoretical calculation. J.Y. provided bulk MnBi_2Te_4 crystals. M.L., C.L., A.H.M., and C.-K.S. analyzed the data. M.L., A.H.M., and C.-K.S. wrote the paper with input from all the authors.

Competing Interest Statement

The authors declare no competing interest.

References

1. R. Li, J. Wang, X.-L. Qi, S.-C. Zhang, Dynamical axion field in topological magnetic insulators. *Nature Physics* **6**, 284-288 (2010).
2. R. S. K. Mong, A. M. Essin, J. E. Moore, Antiferromagnetic topological insulators. *Physical Review B* **81**, 245209 (2010).
3. Y. Tokura, K. Yasuda, A. Tsukazaki, Magnetic Topological Insulators. *Nature Rev. Phys.* **1**, 126 (2019).
4. R. Yu *et al.*, Quantized Anomalous Hall Effect in Magnetic Topological Insulators. *Science* **329**, 61 (2010).
5. C.-Z. Chang *et al.*, Experimental Observation of the Quantum Anomalous Hall Effect in a Magnetic Topological Insulator. *Science* **340**, 167-170 (2013).

6. I. Lee *et al.*, Imaging Dirac-Mass Disorder from Magnetic Dopant Atoms in the Ferromagnetic Topological Insulator $\text{Cr}_x(\text{Bi}_{0.1}\text{Sb}_{0.9})_{2-x}\text{Te}_3$. *Proc. Natl. Acad. Sci. U. S. A.* **112**, 1316 (2015).
7. Y. S. Hor *et al.*, Development of ferromagnetism in the doped topological insulator $\text{Bi}_{2-x}\text{Mn}_x\text{Te}_3$. *Physical Review B* **81**, 195203 (2010).
8. M. M. Otrokov *et al.*, Highly-ordered wide bandgap materials for quantized anomalous Hall and magnetoelectric effects. *2D Materials* **4**, 025082 (2017).
9. M. M. Otrokov *et al.*, Prediction and observation of an antiferromagnetic topological insulator. *Nature* **576**, 416-422 (2019).
10. J. Li *et al.*, Intrinsic magnetic topological insulators in van der Waals layered MnBi_2Te_4 -family materials. *Science Advances* **5**, eaaw5685 (2019).
11. W. Ning, Z. Mao, Recent advancements in the study of intrinsic magnetic topological insulators and magnetic Weyl semimetals. *APL Materials* **8**, 090701 (2020).
12. C. Hu *et al.*, A van der Waals antiferromagnetic topological insulator with weak interlayer magnetic coupling. *Nature Communications* **11**, 97 (2020).
13. C. Liu *et al.*, Robust axion insulator and Chern insulator phases in a two-dimensional antiferromagnetic topological insulator. *Nature materials* **19**, 522-527 (2020).
14. J. Ge *et al.*, High-Chern-number and high-temperature quantum Hall effect without Landau levels. *National Science Review* **7**, 1280-1287 (2020).
15. Y. Deng *et al.*, Quantum anomalous Hall effect in intrinsic magnetic topological insulator MnBi_2Te_4 . *Science* **367**, 895-900 (2020).
16. Y.-F. Zhao *et al.*, Even–Odd Layer-Dependent Anomalous Hall Effect in Topological Magnet MnBi_2Te_4 Thin Films. *Nano Letters* **21**, 7691-7698 (2021).
17. L. Tai *et al.*, Distinguishing two-component anomalous Hall effect from topological Hall effect in magnetic topological insulator MnBi_2Te_4 . *arXiv preprint arXiv:2103.09878* (2021).
18. J. Cui *et al.*, Transport properties of thin flakes of the antiferromagnetic topological insulator MnBi_2Te_4 . *Physical Review B* **99**, 155125 (2019).
19. D. Ovchinnikov *et al.*, Intertwined Topological and Magnetic Orders in Atomically Thin Chern Insulator MnBi_2Te_4 . *Nano Letters* **21**, 2544-2550 (2021).
20. C. Liu *et al.*, Magnetic-field-induced robust zero Hall plateau state in MnBi_2Te_4 Chern insulator. *Nature Communications* **12**, 4647 (2021).
21. M. Otrokov *et al.*, Unique thickness-dependent properties of the van der Waals interlayer antiferromagnet MnBi_2Te_4 films. *Physical review letters* **122**, 107202 (2019).
22. C. Lei, S. Chen, A. H. MacDonald, Magnetized topological insulator multilayers. *Proceedings of the National Academy of Sciences* **117**, 27224-27230 (2020).
23. Y. J. Chen *et al.*, Topological Electronic Structure and Its Temperature Evolution in Antiferromagnetic Topological Insulator MnBi_2Te_4 . *Physical Review X* **9**, 041040 (2019).
24. Y.-J. Hao *et al.*, Gapless Surface Dirac Cone in Antiferromagnetic Topological Insulator MnBi_2Te_4 . *Physical Review X* **9**, 041038 (2019).
25. X. Wu *et al.*, Distinct Topological Surface States on the Two Terminations of MnBi_4Te_7 . *Physical Review X* **10**, 031013 (2020).
26. Y. Yuan *et al.*, Electronic States and Magnetic Response of MnBi_2Te_4 by Scanning Tunneling Microscopy and Spectroscopy. *Nano Letters* **20**, 3271-3277 (2020).
27. P. M. Sass, J. Kim, D. Vanderbilt, J. Yan, W. Wu, Robust A-Type Order and Spin-Flop Transition on the Surface of the Antiferromagnetic Topological Insulator MnBi_2Te_4 . *Physical review letters* **125**, 037201 (2020).
28. Z. Liang *et al.*, Mapping Dirac fermions in the intrinsic antiferromagnetic topological insulators $(\text{MnBi}_2\text{Te}_4)(\text{Bi}_2\text{Te}_3)_n$ ($n=0,1$). *Physical Review B* **102**, 161115 (2020).
29. D. Nevola *et al.*, Coexistence of Surface Ferromagnetism and a Gapless Topological State in MnBi_2Te_4 . *Physical Review Letters* **125**, 117205 (2020).

30. B. Li *et al.*, Competing Magnetic Interactions in the Antiferromagnetic Topological Insulator MnBi₂Te₄. *Physical Review Letters* **124**, 167204 (2020).
31. Y. Lai, L. Ke, J. Yan, R. D. McDonald, R. J. McQueeney, Defect-driven ferrimagnetism and hidden magnetization in MnBi₂Te₄. *Physical Review B* **103**, 184429 (2021).
32. Y. Liu *et al.*, Site Mixing for Engineering Magnetic Topological Insulators. *Physical Review X* **11**, 021033 (2021).
33. M. Garnica *et al.*, Native point defects and their implications for the Dirac point gap at MnBi₂Te₄(0001). *npj Quantum Materials* **7**, 7 (2022).
34. T. Hirahara *et al.*, Large-Gap Magnetic Topological Heterostructure Formed by Subsurface Incorporation of a Ferromagnetic Layer. *Nano Lett.* **17**, 3493 (2017).
35. E. D. L. Rienks *et al.*, Large Magnetic Gap at the Dirac Point in Bi₂Te₃/MnBi₂Te₄ Heterostructures. *Nature* **576**, 423 (2019).
36. S. Wimmer *et al.*, Mn-Rich MnSb₂Te₄: A Topological Insulator with Magnetic Gap Closing at High Curie Temperatures of 45–50 K. *Advanced Materials* **33**, 2102935 (2021).
37. P. Küppers *et al.*, Probing the magnetic band gap of the ferromagnetic topological insulator MnSb₂Te₄. *arXiv preprint arXiv:2202.11540* (2021).
38. D. S. Lee *et al.*, Crystal Structure, Properties and Nanostructuring of a New Layered Chalcogenide Semiconductor, Bi₂MnTe₄. *CrystEngComm* **15**, 5532 (2013).
39. Z. Huang, M.-H. Du, J. Yan, W. Wu, Native defects in antiferromagnetic topological insulator MnBi₂Te₄. *Physical Review Materials* **4**, 121202 (2020).
40. M. H. Du, J. Yan, V. R. Cooper, M. Eisenbach, Tuning Fermi Levels in Intrinsic Antiferromagnetic Topological Insulators MnBi₂Te₄ and MnBi₄Te₇ by Defect Engineering and Chemical Doping. *Advanced Functional Materials* **31**, 2006516 (2021).
41. A. A. Khajetoorians *et al.*, Detecting excitation and magnetization of individual dopants in a semiconductor. *Nature* **467**, 1084-1087 (2010).
42. A. A. Khajetoorians *et al.*, Spin Excitations of Individual Fe Atoms on Pt(111): Impact of the Site-Dependent Giant Substrate Polarization. *Physical Review Letters* **111**, 157204 (2013).
43. C. F. Hirjibehedin, C. P. Lutz, A. J. Heinrich, Spin Coupling in Engineered Atomic Structures. *Science* **312**, 1021-1024 (2006).
44. C. Lei, A. H. MacDonald, Gate-tunable quantum anomalous Hall effects in MnBi₂Te₄ thin films. *Physical Review Materials* **5**, L051201 (2021).
45. J.-Q. Yan *et al.*, Crystal growth and magnetic structure of MnBi₂Te₄. *Physical Review Materials* **3**, 064202 (2019).
46. J. Yan, The elusive quantum anomalous Hall effect in MnBi₂Te₄: a materials perspective. *arXiv preprint arXiv:2112.09070* (2021).
47. G. Kresse, J. Hafner, Ab initio molecular dynamics for liquid metals. *Physical Review B* **47**, 558-561 (1993).
48. J. P. Perdew, K. Burke, M. Ernzerhof, Generalized Gradient Approximation Made Simple. *Physical Review Letters* **77**, 3865-3868 (1996).
49. B. Himmetoglu, A. Floris, S. de Gironcoli, M. Cococcioni, Hubbard-corrected DFT energy functionals: The LDA+U description of correlated systems. *International Journal of Quantum Chemistry* **114**, 14-49 (2014).

Figures

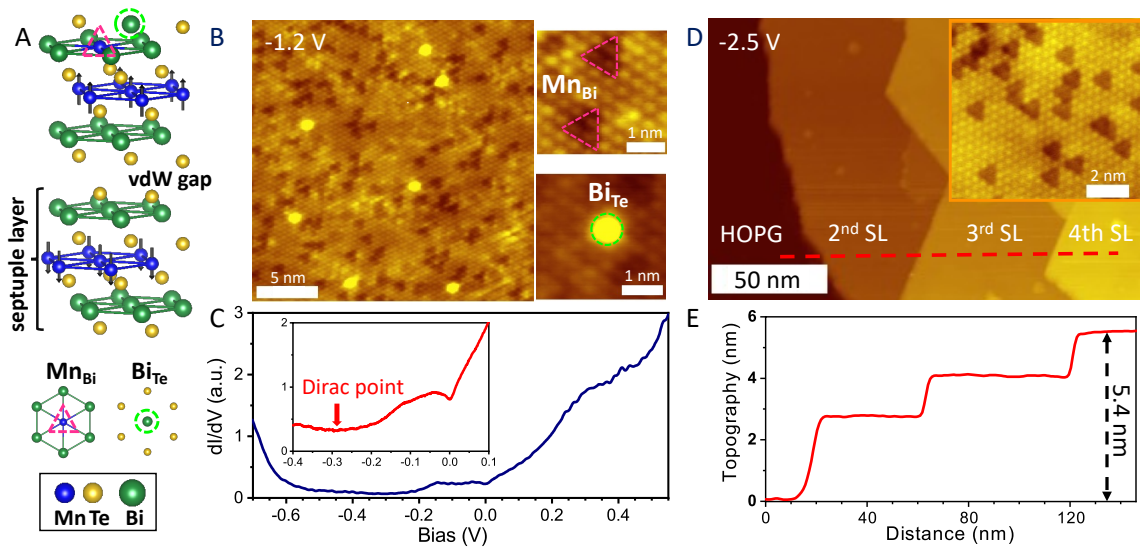


Fig. 1. Bulk crystals versus MBE grown thin films. (A), Crystal structure of MnBi₂Te₄. The black arrows illustrate the intralayer ferromagnetic and interlayer antiferromagnetic coupling. Cleave plane happens at the van der Waals gap. Mn_{Bi} and Bi_{Te} antisite defects are outlined with a pink triangle, and green circle. (B), Atomic image taken on Te truncated bulk MnBi₂Te₄ surface. Examples of Mn_{Bi} and Bi_{Te} antisites are outlined by pink triangles and green circles. (C), STS taken on bulk MnBi₂Te₄ surface. Inset red curve shows zoom-in bias range. The red arrow marks the Dirac point. (D), Topographic image taken on MBE-grown MnBi₂Te₄. Inset shows its atomic image. (E), Topographic cross-section along the red dashed line on D shows the thickness of each SL is 1.35 nm.

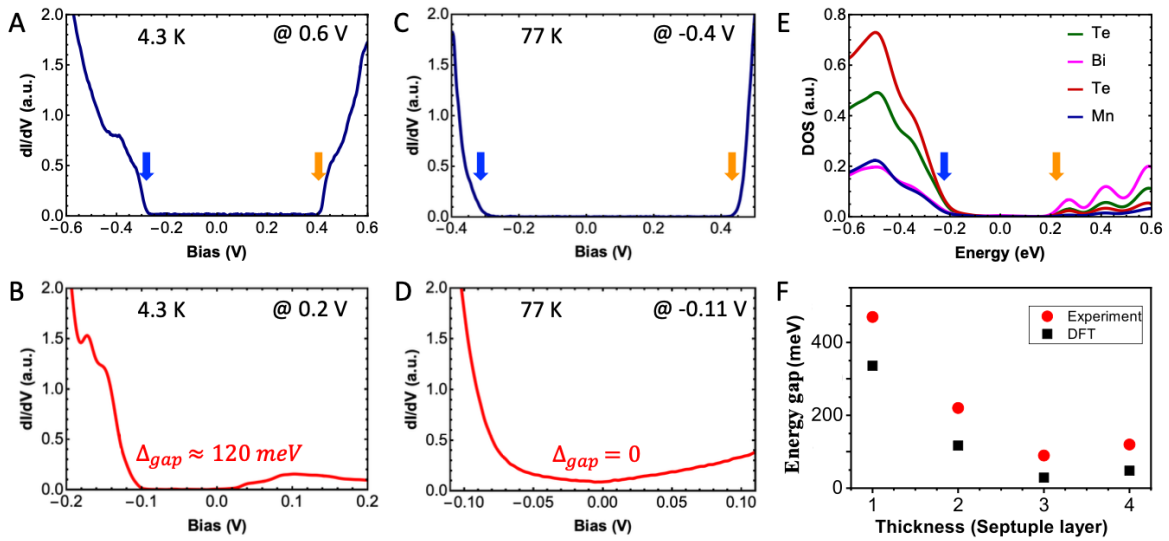


Fig. 2. Direct observation of Dirac mass gap. (A,B), STS taken on 4 SL MnBi₂Te₄ at 4.3 K with a 0.6 V and 0.2 V setpoint biases. STS in B shows a ~ 120 meV Dirac mass gap. (C,D), STS taken on 4 SL MnBi₂Te₄ at 77 K with a -0.4 V and -0.11 V setpoint biases. STS in D shows that the Dirac mass gap has disappeared. (E), DFT calculated DOS for 4 SL MnBi₂Te₄ with a projection to the topmost four atomic layers. Blue and orange arrows on A, C, and E mark the threshold energies that bound the low-conductance bias region. (F), Summarized STS-measured and DFT-calculated energy gap as a function of film thickness.

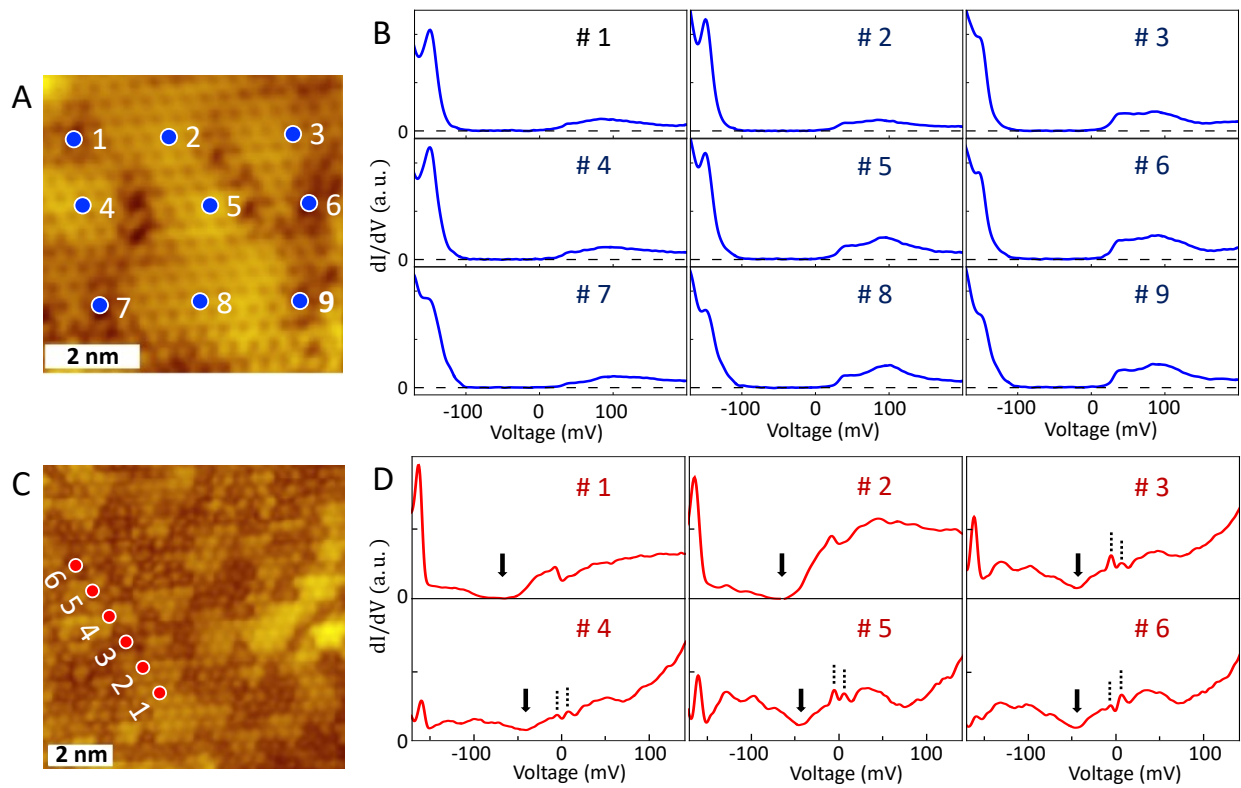


Fig. 3. Dirac mass gap variation as a function of defect distribution. (A), Atomic image taken on low defect 4 SL region (setpoint bias: 0.3 V). (B), Spatial-dependent STS distribution with spatial locations marked on A. Horizontal black dashed lines mark zero. (C), Atomic image taken on high defect 3 SL region (setpoint bias: -0.35 V). (D), Spatial-dependent STS distribution with spatial locations marked on C. Black arrows mark the Dirac point. Vertical black dashed lines on STS #3 to #6 mark the zero-bias tunneling anomaly.

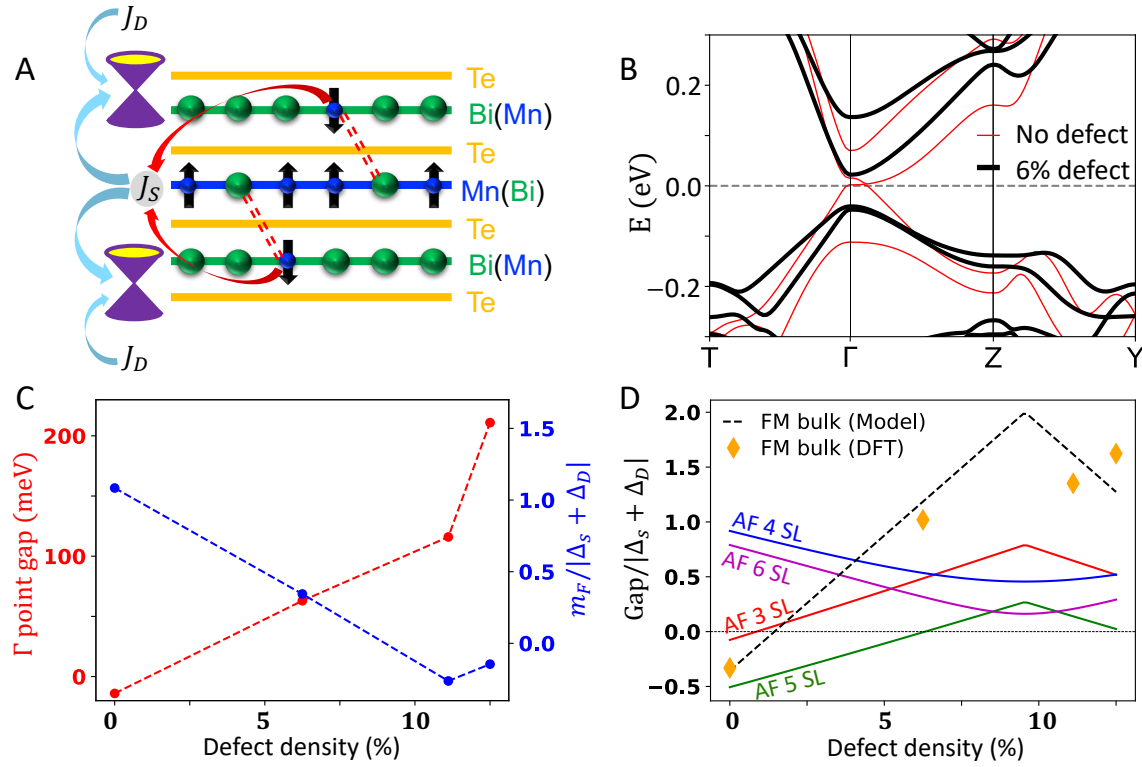


Fig. 4. *Ab initio* DFT calculation and coupled Dirac cone model. (A), Schematics for magnetic moments configuration and exchange couplings between the Dirac cones and the local magnetic moments. Both the Mn_{Bi} antisites and Mn layer contribute to the exchange coupling. Red dashed lines illustrate the next nearest-neighboring antisites pairs. (B), Calculated band dispersion for ferromagnetic bulk MnBi₂Te₄ in defect-free and 6% Mn_{Bi} antisites cases. (C), DFT calculated Γ point energy gap and extracted model parameter m_F as a function of Mn_{Bi} antisites defect density. Negative gap values represent inverted bands. (D), Coupled Dirac cone model-calculated Γ point energy gap as a function of Mn_{Bi} antisites defect density in the case of ferromagnetic (FM) bulk and antiferromagnetic (AF) thin films. DFT calculated FM bulk results are plotted in orange diamonds. FM (AF) refers to spin moments in Mn layers being aligned (anti-aligned) between adjacent septuple layers.

Supplementary Information for

Visualizing the interplay of Dirac mass gap and magnetism at nanoscale in intrinsic magnetic topological insulators

Mengke Liu¹, Chao Lei¹, Hyunsue Kim¹, Yanxing Li¹, Lisa Frammolino¹, Jiaqiang Yan²,
Allan H. Macdonald^{1*}, Chih-Kang Shih^{1*}

* To whom correspondence may be addressed.

Email: macdpc@physics.utexas.edu or shih@physics.utexas.edu.

This PDF file includes:

Figures S1 to S8

Details on coupled Dirac cone model and DFT supercells

Additional discussion on magnetic antisites effect in odd and even septuple layers

Fig. S1

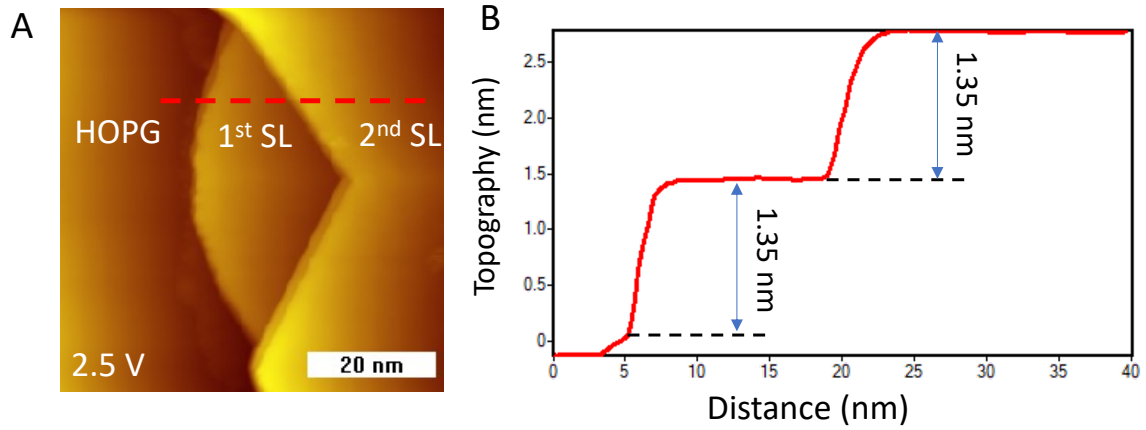


Fig. S1. Additional data on MBE grown MBT on HOPG substrate. (A), Topographic image taken on MBE-grown MBT showing the 1st and 2nd septuple layers (SLs). (B), Topographic cross section along the red dashed line on a showing the step height of each septuple layer is 1.35 nm.

Fig. S2

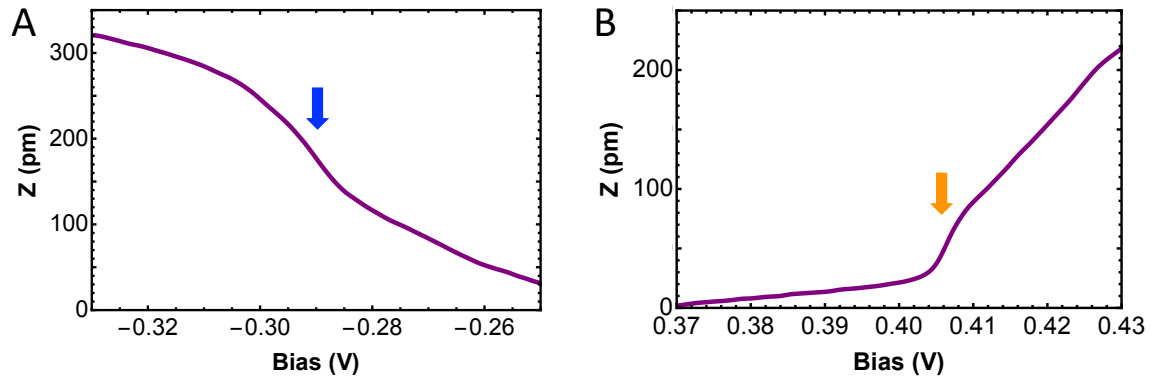


Fig. S2. Characterization of tip-to-sample distance (Z) behavior at different biases. (A,B), constant-current Z - V spectra at negative and positive biases show a Z jump at energies marked by blue and orange arrows. This Z -jump indicates a reduced tip-to-sample distance due to a reduced conductance. These two critical energies here coincide with the two thresholds in dI/dV spectra shown in Fig. 2A, confirming the reduced density-of-state bias region as discussed in the main text.

Fig. S3

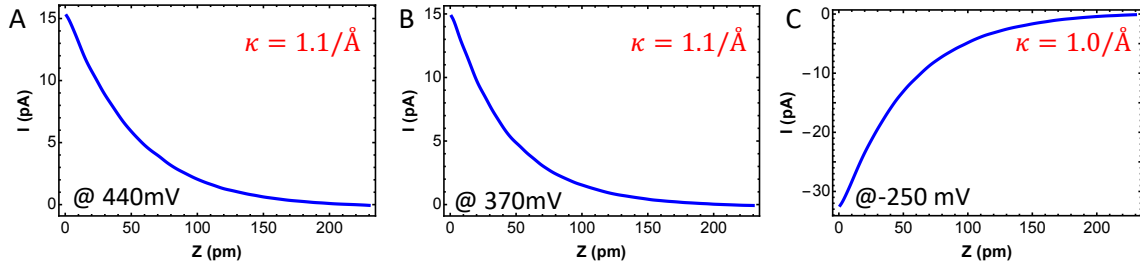


Fig. S3. Characterization of tunneling barrier condition at different setpoint biases. (A-C), I - Z spectra demonstrating the decay constant of the tunneling barrier at different setpoint biases. I denotes the tunneling current. Z denotes the tip-to-sample distance. The measured decay constant κ from these I - Z spectra is $1.1/\text{\AA}$ at 440 mV and 370 mV, $1.0/\text{\AA}$ at -250 mV, indicating normal vacuum tunneling barriers above and below the threshold energies. This set of tunneling barrier characterization ensures that the dI/dV spectra in Fig. 2 are carried out in vacuum tunneling conditions without tip-to-sample interactions, thus confirming the reliability of the dI/dV spectra.

Fig. S4

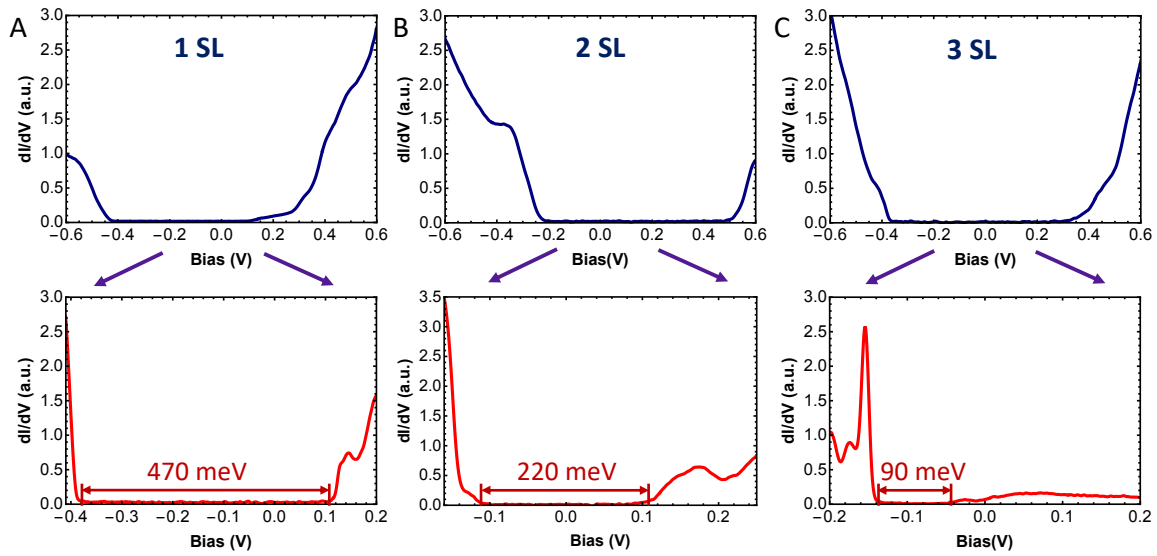


Fig. S4. STS on different septuple layer MBT showing thickness-dependent energy gap. (A), STS taken on 1 SL showing 470 meV gap. (B), STS taken on 2 SL showing 220 meV gap. (C), STS taken on 3 SL showing 90 meV gap.

Fig. S5

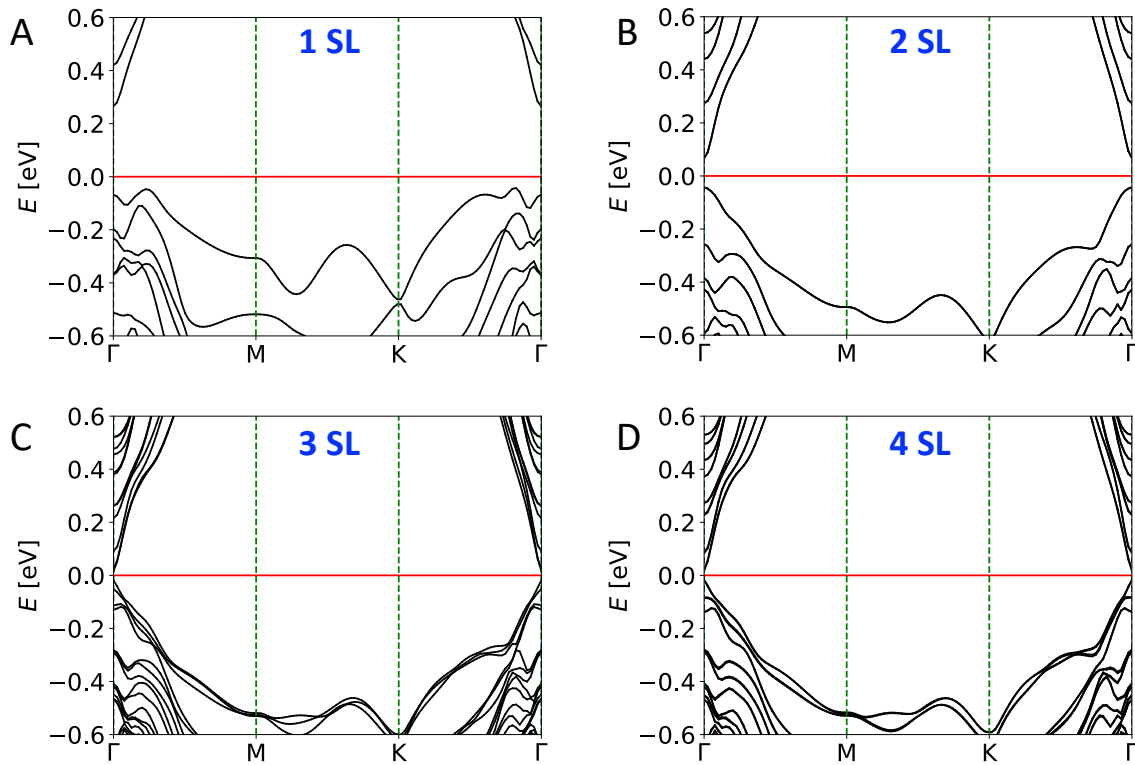


Fig. S5. DFT calculated MBT thin film band structures. (A-D), DFT calculated 1 SL to 4 SL MBT band structure. The calculated energy gap is: 336 meV (1SL), 117 meV (2 SL), 29 meV (3 SL), 48 meV (4 SL).

Details on Coupled Dirac cone model and DFT supercells

We employed the coupled Dirac cone model (Ref. 22 in main text) that includes only Dirac cone surface states on the top and bottom surfaces of each septuple layer and hoppings between Dirac cones.

The Hamiltonian is expressed as:

$$H = \sum_{k_{\perp}, ij} [((-)^i \hbar v_D (\hat{z} \times \sigma) \cdot k_{\perp} + m_i \sigma_z) \delta_{ij} + \Delta_{ij} (1 - \delta_{ij})] c_{k_{\perp}i}^{\dagger} c_{k_{\perp}j},$$

where i and j are Dirac cone labels, \hbar the reduced Planck constant, and v_D the velocity of the Dirac cones. The parameter m_i is the exchange potential strength of the i th Dirac cone. Hopping from the i th surface to the j th surface is denoted by Δ_{ij} . Here we only retain the most important hybridization parameters indicated by the hopping within the same layer Δ_S , and the hopping across the van der Waals gap between adjacent layers Δ_D ; The total exchange potential in bulk MnBi_2Te_4 for each Dirac cone is $m_F = J_S + J_D$ in the ferromagnetic configuration, and $m_{AF} = J_S - J_D$ in the antiferromagnetic configuration, where J_S and J_D are the exchange couplings from the same layer and the adjacent layer, as illustrated in Fig. S6. The existence of the Mn_{Bi} antisites defects, forming an antiferromagnetic coupling with that in the central Mn layer²³, leading to a reduced same-septuple-layer and neighboring-septuple-layer exchange couplings J_S and J_D . The presence of Bi_{Mn} antisite also decreases J_S by reducing the magnetic moments in the Mn layer.

For the ferromagnetic configuration, the exchange energies are the same in every layer, and the model band energy dispersion along the Γ to Z line is:

$$E(k_Z) = \pm \sqrt{\Delta_S^2 + \Delta_D^2 + 2\Delta_S\Delta_D \cos k_Z d} \pm m_F.$$

The energies at $k_Z d = 0$ and $k_Z d = \pi$ are:

$$E_{\Gamma} = \pm(\Delta_S + \Delta_D) \pm m_F; E_Z = \pm(\Delta_S - \Delta_D) \pm m_F.$$

Comparing with DFT band energies at Γ and Z points, one can extract the model parameters, Δ_S , Δ_D , and m_F .

To estimate the exchange couplings as a function of defect density, $J_S(x)$ and $J_D(x)$ where x denotes the Mn_{Bi} defect density, we performed DFT calculations at a few different Mn_{Bi} antisites densities, 0%, 6%, 11%, 12.5%, as explained in the Methods and Fig. S7. Assuming the ratio between J_D and J_S is independent of the defect density, i.e. $J_D(x) = \delta J_S(x)$, δ turns out to be 0.8, extracted from the DFT calculated results. Fig. 4 demonstrates the exchange coupling m_F decreases nearly linearly with defect density. It is thus reasonable to assume $J_S(x) = J_S^0 - \alpha x$, where J_S^0 is the exchange coupling without defect and α is the linear coefficient. Therefore, the effective exchange potential in bulk MnBi_2Te_4 with ferromagnetic spin configuration can be expressed as:

$$m_F(x) = (1 + \delta)(J_S^0 - \alpha x).$$

We may then extract the value of α from Fig. 3C, a summarized m_F as a function of defect density.

These exchange coupling dependence on the defect density $J_S(x)$ and $J_D(x)$, are then used to perform model calculations for the ferromagnetic bulk and antiferromagnetic thin films, as shown in the main text Fig. 4D.

Fig. S6

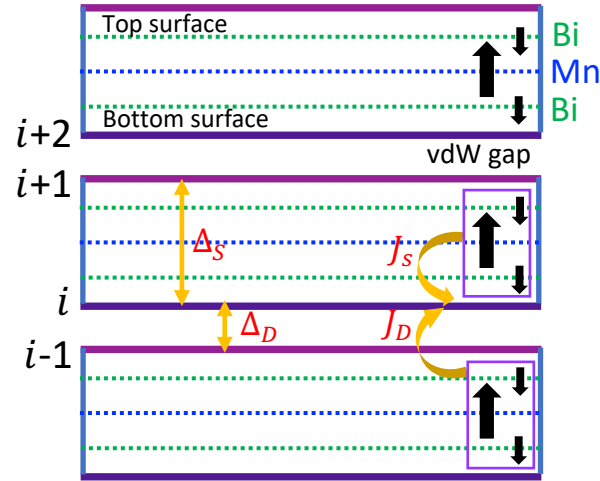


Fig. S6. Schematic illustration of coupled Dirac cone model in the ferromagnetic configuration. Dirac cones localized on each septuple layer's top and bottom surfaces are hybridized with remote Dirac cones. Δ_S denotes hopping parameter between Dirac cones from the same septuple layer. Δ_D denotes hopping parameter between Dirac cones from the adjacent layer across the van der Waals gap. Dirac cones are exchange-coupled to local magnetic moments from their own layer (J_S) and their neighboring layer (J_D). Black arrows represent the local orientation of the magnetic moments. i denotes the layer index. “Ferromagnetic configuration” refers to spin moments in Mn layers being aligned between adjacent septuple layers.

Fig. S7

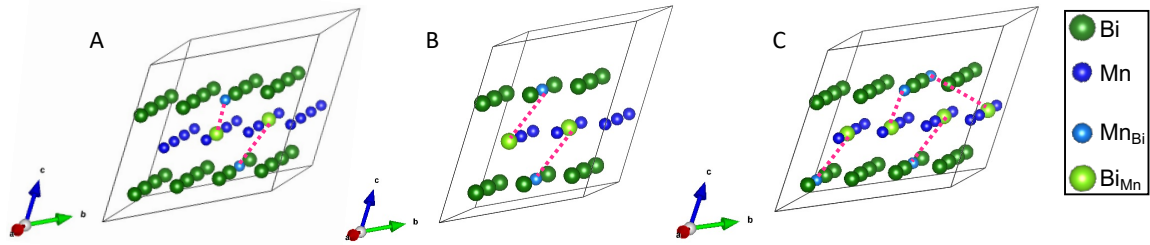


Fig. S7. DFT supercell configurations for bulk MnBi_2Te_4 with antisite defects. (A), A $4 \times 4 \times 1$ supercell configuration corresponding to 6% Mn_{Bi} antisite density. one per sixteen Bi atoms is substituted by its next-nearest neighboring Mn atom. (B), A $3 \times 3 \times 1$ supercell configuration corresponding to 11% Mn_{Bi} antisite density. One per nine Bi atoms is substituted by its next-nearest neighboring Mn atom. (C), A $4 \times 4 \times 1$ supercell configuration corresponding to 12.5% Mn_{Bi} antisite density. Two per sixteen Bi atoms were substituted by their next-nearest neighboring Mn atoms. The red dashed lines connect the next-nearest neighboring Mn_{Bi} and Bi_{Mn} antisites pairs. The antisite defect density in the top and bottom Bi layers are kept the same. Te atoms are left out for simplicity.

Additional discussion on magnetic antisites effect in odd and even septuple layers

Fig. 4D in the main text shows that for odd septuple layers, the Dirac mass gap exhibits a nearly linear suppression as a function of defect density, and a negative gap eventually collapses accompanied by a topological phase transition. However, for even septuple layers, the gap change as a function of defect density at small defect density appears linear and, when close to the minimum (9%), it appears like a quadratic curve. Their gap signs always remain positive, indicating no topological phase transition. Regardless of the gap sign, the absolute value of a gap appears to be more robust against magnetic antisite density in even septuple layers than that in odd septuple layers.

The behavior is under expectation from a toy model that has been discussed by Lei and MacDonald (ref. 44 in main text). Here we recap it below:

Antiferromagnetic MnBi_2Te_4 thin films can be simply illustrated with a model that only considers the two Dirac cones located on the top and bottom surfaces. The two Dirac cones have the same (opposite) sign of mass terms for MBT thin films with an odd (even) number of SLs. For thin films with odd SLs, the Hamiltonian may be written as:

$$H_{odd} = \begin{pmatrix} m & v_D k^+ & \Delta & 0 \\ v_D k^- & -m & 0 & \Delta \\ \Delta & 0 & m & -v_D k^+ \\ 0 & \Delta & -v_D k^- & -m \end{pmatrix},$$

where $k^\pm = k_x \pm i k_y$, v_D is the Dirac velocity, m is the Dirac mass that depends on the exchange coupling, Δ is the hybridization parameter between the two Dirac cones. The eigenvalues are: $E = \pm \sqrt{v_D^2 |k|^2 + (m \pm \Delta)^2}$, where $|k|^2 = k_x^2 + k_y^2$.

In this simplified model, the band gap locates at Γ point, which is $E_{gap}^{odd} = 2(m - \Delta)$. We can see that this gap exhibits a linear dependence on the exchange mass m , and a

topological phase transition appears at $m = \Delta$. Note that we assumed a linear dependence of m on the antisites density, which has been above.

Similarly, for even SLs, the top and bottom Dirac cones have an opposite sign of Dirac mass. The Hamiltonian reads:

$$H_{even} = \begin{pmatrix} m & v_D k^+ & \Delta & 0 \\ v_D k^- & -m & 0 & \Delta \\ \Delta & 0 & -m & -v_D k^+ \\ 0 & \Delta & -v_D k^- & m \end{pmatrix},$$

It has eigenvalues as $E = \pm \sqrt{v_D^2 |k|^2 + m^2 + \Delta^2}$, and band gap as $E_{gap}^{even} = 2\sqrt{m^2 + \Delta^2}$.

We see that in this case the gap is always positive indicating the disappearance of the topological phase transition. The gap minimizes at $m = 0$, where the exchange splitting contributed by antisites fully cancels that from the central Mn layer. A Taylor expansion around this local minimum shows quadratic behavior. Far away from this local minimum where $|m| > \Delta$, such a gap appears to be linearly dependent on m .

Fig. S8 plots band structure evolution as a function of exchange mass m to visualize the energy gap change as a function of m in odd and even SLs, demonstrating the topological phase transition and the sensitivity to exchange mass of the energy gap in odd SLs films.

Fig. S8

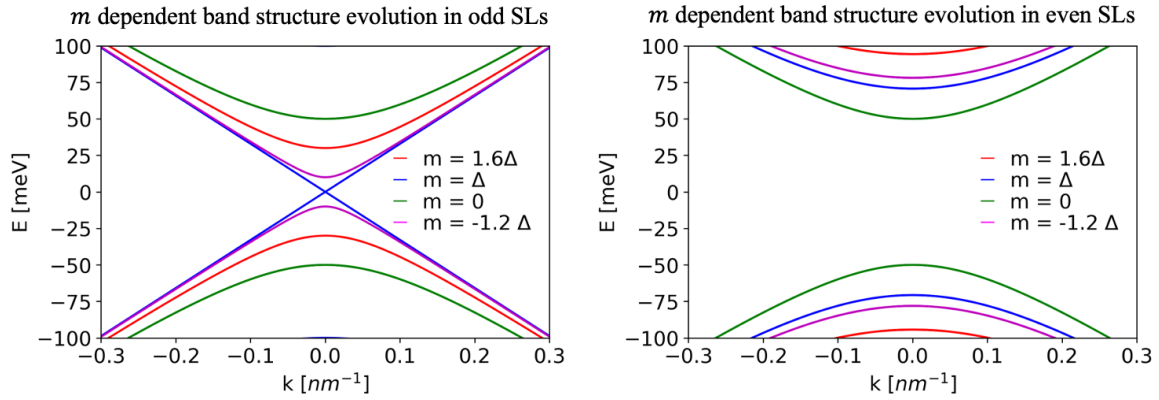


Fig. S8. Band structure evolutions as a function of exchange mass m , in antiferromagnetic MBT thin films. (Left) Odd septuple layer thickness. (Right) even septuple layer thickness. m is parametrized in the magnitude of the hybridization parameter Δ , and Δ is chosen to be 50 meV.